ECS Journal of Solid State
Science and Technology

The Electrochemical Society
Advancing solid state & electrochemical science & technology

Tunable Etching of CVD Graphene for Transfer Printing of Nanoparticles Driven by Desorption of Contaminants with Low Temperature Annealing

To cite this article: L. S. Hui *et al* 2020 *ECS J. Solid State Sci. Technol.* **9** 093006

ECS Journal of Solid State Science and Technology, 2020 **9** 093006

Tunable Etching of CVD Graphene for Transfer Printing of Nanoparticles Driven by Desorption of Contaminants with Low Temperature Annealing

L. S. Hui,[1] M. Munir,[1] E. Whiteway,[2] An. Vuong,[2] M. Hilke,[2] V. Wong,[3] G. Fanchini,[3] and A. Turak[1,z]

[1]*Department of Engineering Physics, McMaster University, Hamilton, Ontario, L8S 4L7, Canada*
[2]*Department of Physics, McGill University, Montreal H3A 2T8, Canada*
[3]*Department of Physics and Astronomy, University of Western Ontario, London, Ontario N6G 2V4, Canada*

Due to its exceptional mechanical properties, graphene can be an ideal support for nanotransfer printing. However, in its as-received state, it is incompatible with some processes for preparing 2D arrays of colloidal nanoparticles from reverse micelle templating. By treating CVD graphene with low temperature annealing, we have created a universal carrier to transfer such nanoparticles onto organic surfaces, taking advantage of the activation of the graphene surface via oxygen plasma etching. Desorption of hydrocarbon contaminant species by low temperature annealing is essential to ensure that exposure of the CVD graphene to the plasma oxidizes the film rather than etching it, as confirmed by Raman, Attenuated Total Reflectance- Fourier Transform Infrared (ATR-FTIR), and X-ray photoelectron spectroscopy measurements. Upon transfer printing to an organic surface, the nanoparticles are sandwiched between the reduced graphene oxide-like layer and the organic surface as shown by scanning near-field optical microscopy (SNOM), making them ideal as an interlayer in organic devices. The combination of exposure to plasma and annealing gives two vectors for controlling the oxygen doping profile in the activated graphene on Cu, and suggests new avenues for patterning nanostructures in devices with processing sensitive active layers.
[DOI: 10.1149/2162-8777/aba855]

Manuscript submitted June 14, 2020; revised manuscript received July 16, 2020. Published July 31, 2020. *This paper is part of the JSS Focus Issue on 2D Layered Materials: From Fundamental Science to Applications.*

Supplementary material for this article is available online

A variety of advanced technological fields, including organic photovoltaics, display devices, sensors, photonics, micromechanical systems, microfluidics and microelectronics[1–8] have benefitted from the incorporation of 2D arrays of nanostructures. Di-block copolymers, due to their amphiphilic nature, spontaneously form core-corona micelles in selective solvents. Using the micelles as "nanoreactors" allows the formation of highly size controllable nanoparticles, with less than 2% deviation in the average particle diameter.[3,5,9,10] Such nanoparticles are ideal for electronic devices as the bottleneck in the development of nanoparticle based applications lies in heterogenity and uneven spatial distributions.[11] However, incorporation of precise planar arrangements of solution derived colloidal nanoparticles into the fabrication stream of oxygen sensitive organic and perovskite electronic devices is challenging. The use of oxygen or inert gas plasma to remove the polymer shell from around the nanoparticle generally damages the fragile active layers, if deposited directly.

A key approach to incorporating nanostructures into device involves the use of nanotransfer printing methods, which generally either use a "pick-and-release" method with an elastomeric stamp,[2,12,13] or a sacrificial carrier layer with high mechanical strength.[14,15] Stiffer materials can be made thinner and maintain the desired pattern while withstanding external peeling forces. Thus, a high Young's modulus is critical for the replication of nanoscale features and patterns.[16] The exceptionally high stiffness of graphene makes it an excellent transfer layer candidate, and many groups have successfully transferred layers as large as 20 cm^2 consisting of high quality, crackless chemical vapor deposited (CVD) graphene.[17–19] Using these well-developed graphene transfer methods, one can make use of the graphene layer to carry the nanoparticles to the target substrate for nanotransfer printing. However, in such a case the prolonged plasma dosage that is adequate to destroy the reverse micelles would also need to be applied to the graphene layer.

We have recently shown that graphene on Cu produced by chemical vapor deposition (CVD) behaves very differently under direct oxygen plasma bombardment compared to free standing graphene and graphene supported on other substrates,[20] forming reduced graphene oxide (rGO)-like structures. Due to the synergistic oxidation mechanism between graphene and the underlying Cu, the degree of oxygen functionalization can be effectively tuned with the oxygen plasma dose.[20]

In rGO and graphene oxide (GO), epoxide groups at the bridges or top sites of the graphene basal plane[21–23] causes the sp^2-hybridized honeycomb carbon network to be perturbed.[23,24] Depending on the degree of attachments of oxygen functional groups, the optoelectronic properties of the functionalized graphene can be effectively controlled.[25,26] Increasing the proportion of carbonyl and hydroxyl groups, which alters the projected density of states of the carbon atoms in rGO,[27] can increase the work-function, decrease the conductivity over many orders of magnitude and shift the photoluminescent (PL) emission peak into the red.[26–28] The versatility of rGO as a semiconductor material is therefore of great interest if one can effectively tune and functionalize the material in a controlled manner, which is technically challenging.[27]

This combination of high mechanical strength and unique electronic properties under plasma etching make CVD graphene the ideal transfer medium for micelle templated nanoparticles. However, predictable oxidation generally requires a relatively clean surface, free of contaminants. Graphene is easily doped by adsorption of oxygen in ambient environments which modify the wettability, carrier mobility, adhesion, and charge doping.[29–32] As little as 20 min exposure to ambient environments is sufficient to make freshly grown CVD graphene on Cu significantly more hydrophobic.[29] Due to this strong affinity, contaminant sources are ubiquitous, even in high end nanofabrication facilities,[33] from the volatile organic compounds (VOC) emitted by common plastic-ware such as plastic petri dishes[34] or sample boxes,[33] to organic solvents and plasticizers[35] to even the quality of the quartz tube during fabrication.[36]

[z] E-mail: turaka@mcmaster.ca

In this contribution, we shows that the presence of oxygen contaminants compromises the tunability of functionalized rGO-like surfaces using a plasma. Using Raman and Attenuated Total Reflection- Fourier Transform Infrared (ATR-FTIR) spectroscopy, we examined the surface composition of as-received, plasma-oxidized, plasma-etched and annealed samples. The Raman analysis confirms that similar rGO-like structures are formed on the surface during plasma oxidation. Low temperature annealing, through decontamination of the surface, improves the resilience of CVD graphene, allowing it to be used as a universal carrier to transfer micelle templated nanoparticles onto organic surfaces. The activated graphene that results from the plasma etching provides a mechanical and environmental barrier suitable to transfer a variety of nanoparticle types, paving new avenues for patterning nanostructures while simultaneously introducing functionalized graphene into electronic devices.

Experimental

Graphene was synthesized by CVD on commercially available 25 μm copper foils (Alfa Aesar). The foils were first chemically treated with acetic acid and annealed for 4 hours at 1078 °C under a flow of 8 sccm hydrogen gas in order to clean the copper surface. Growth temperature was maintained at 1078 °C during a 4 min CVD growth phase where gas flows of 1.2 sccm methane were introduced. In order to ensure the same aging of all samples, they were taken from the same graphene master, which was stored in a desiccator in vacuum. Samples were annealed on a hotplate (Barnstead Thermolye Super-Nuova) at 180 °C for 4, 15, 22.5, 30, 45 and 60 mins (designated *AT*X, where X indicates time in minutes). They were allowed to cool before further processing. Each sample was plasma etched (Harrick Plasma PDC-00) at 29.6W in 30 sccm oxygen (Alphagaz, 99.999%) for various times (designated *ET*X, where X indicates time in minutes).

LiF nanoparticles were synthesized using the reverse micelle templating method, as described previously.[3,4] Briefly, poly(styrene-*b*-2-vinyl pyridine) di-block copolymer (Polymer Source Inc.) was dissolved in reagent grade o-xylene, with a concentration of 3mg/ml under continuous stirring. Precursors LiOH and HF were added sequentially to the reverse micelles solutions, with a time interval of 24 h to allow thorough infiltration of each precursor. The final loaded reverse micelles solution was centrifuged to remove excess, non-infiltrated salt and stirred further to prevent coagulation.

To transfer the nanoparticles onto an organic surface, a direct printing method developed by Feng et al.[37] was adopted. The reverse micelles loaded with precursors are spin-coated onto the treated CVD graphene substrates, and plasma etched in oxygen to remove the polymeric shell. The target organic layer is then spin-coated onto the etched surface, and cured according to the manufacturer instructions. Once fully prepared, the whole stack of material is floated onto a Cu etchant solution to dissolve the Cu. The process is followed by displacing the Cu with deionized water to wash away any Cu etchant residue . To recover the stack from the water, glass or ITO-coated-glass is lowered on top of the stack and allowed to attach. Finally, the stack is flipped. The final rGO/nanoparticles/organic layer/ITO is allowed to dry in a N_2 filled glove box environment.

Transmission-mode scanning near-field optical microscopy (SNOM) is used with the goal of validating the successful transfer printing of nanoparticles in contact with the organic surface, underneath the transferred rGO-like layer. This is not possible with conventional atomic force microscopy (AFM) because AFM is only sensitive to the top surface of graphene. Conversely, due to the sub-surface sensitivity of aperture-type SNOM, nanoparticles attached to the bottom surface of graphene can be detected.[38] Aperture-type SNOM measurements are carried out by a sub-wavelength 90-nm aperture micromachined through a contact-mode AFM cantilever. In this way, sub-surface sensitivity at penetration depths of the order of the aperture diameter (i.e. 90 nm) underneath the scanned surface can be achieved. Lateral resolution of the same order of magnitude (i.e. 90 nm, or better) can also be obtained, well beyond the limit of diffraction. Transmission SNOM measurements were carried out using a Witec Alpha 300S microscope equipped with aperture-type cantilevers (NT-MDT Inc.) in which conventional contact-mode AFM scans can be simultaneously acquired along with nano-optical SNOM scans. For SNOM, a 532 nm laser (Excelsior, Spectra Physics, 80 mW) is focused on the aperture apex of the hollow AFM cantilever by an upright confocal optical microscope. The transparent sample is positioned onto the AFM piezoelectric scanner and near-field radiation is collected by an inverted microscope below, while the sample is scanned by the AFM tip. Light is conveyed to a Hamamatsu photomultiplier tube (PMT) connected to the inverted microscope through an optical fiber. At the same time, each pixel produces an AFM image through a force sensor to which the hollow cantilever is attached.

ATR-FTIR was collected on a Bruker Vertex 70 FTIR equipped with the Platinum Diamond ATR apparatus, using the standard mid-IR laser (Globar). The measurements were accumulated for 152 scans with a 4 cm^{-1} resolution and collected with a RT DLaTGS detector. The output spectrum was subtracted against the background environment spectrum.

The XPS spectra were generated by a monochromated Al K source with a photon energy of 1486.6 eV at a pass energy of 25.00 eV (Thermo K-Alpha). The spot size was 400 μm^2. The XPS measurements were not charge corrected, given the samples were highly conductive and peak charging was insignificant. The XPS spectra was analyzed with the Thermo Avantage software tool with the Smart background correction option, which is based on the Shirley background correction method. The peaks were then fitted with Voigt (Gaussian-Lorentzian) functions.

Raman measurements were performed at 514 nm laser excitation and laser power set at 20 mW (Renishaw inVia). This power was low enough to prevent any laser modification of the sytstem. Raman data were processed with OMNIC Series (Thermo Fisher Scientific) and the deconvolution procedures were performed with OriginPro 8 (OriginLab), as described previously.[20] Briefly, the Cu florescent background under 514 nm excitation was first removed and the resulting spectrum features deconvoluted using Lorentzian line shape profiles. For non-etched samples, the G mode was treated as one single peak at 1580 cm^{-1} whereas for etched samples, the G mode is denoted as G_{app} mode due to the convolution of the original G mode with a defect D′ mode. The G_{app} mode was set at the 1590 cm^{-1} position and the D′ mode near 1620 cm^{-1} was extracted from the least squares fitting routine. D and 2D modes were fitted as a single Lorentzian peak respectively at near 1350 cm^{-1} and 2690 cm^{-1}. Error analysis was evaluated by standard deviation of peaks among the same set of sample variations.

Contact angle measurements were performed with the Kruss Drop Shape Analyzer-DSA100, using a 26 s gauge (0.474 mm outer diameter) flat needle for 10 μl water droplet dispensing. Samples of full graphene aged for the same amount of time were annealed in air for 0, 4, 15, 30, 60 min at 180 °C on a hotplate. The samples after annealing were immediately kept in a glass Petri dish and stored under vacuum prior to measurement, to avoid airborne contamination. Each sample was recorded for 50 s with 1 s intervals. The contact angle is measured from the sessile drop image at the points of intersection between the drop contour and the baseline which is the sample surface. The final contact angle of each sample is an average of the 100 measurements from both left and right sides of the droplet images.

Results and Discussions

The micelle templated deposition (RMD) process requires sustained plasma etching to produce monodisperse nanoparticles, as shown in supporting info Fig. A-1 (available online at stacks.iop.org/JSS/9/093006/mmedia). In a plasma, the highly energetic ions bombard the surface, displacing surface bonded species within the collision cascade and creating dangling bonds where incident radicals may then chemisorb[39] or chemically etch a carbon network. Typically, 25 min of oxygen plasma is enough to remove the copolymer shell, exposing the nanoparticles, though the particle size and dispersion are roughly unchanged even with sustained etching.

However, this level of etching is typically also destructive to organic semiconductor surfaces (see supporting info Fig. A-2), preventing the direct deposition of such nanoparticles for organic electronic devices. To introduce the nanoparticles onto a fragile oxygen and plasma sensitive surface, a high mechanical strength carrier layer such as graphene would be useful. Yet, as graphene is also a carbon network, high plasma dosages are also typically destructive to graphene.[20,40,41] The critical etching time (CET) for CVD graphene on Cu (FG) has been previously established as the time in minutes required for the total disappearance of all the Raman modes of graphene,[20,42] indicating complete removal of graphene from the Cu surface. Exposure to oxygen plasma for less than the CET results in a reduced graphene oxide (rGO)-like network,[20] where the oxygen content can be tuned by the etching process.

This is shown in the high resolution *C* 1*s* XPS spectra in Fig. 1. As expected for graphene and rGO, the *C* 1*s* signal at 285.1 eV can be deconvoluted into sp^3 and sp^2 carbon bonds.[43–47] For the pristine (*AT*0*ET*0 black crosses in Fig. 1a) and annealed unetched graphene sample (*AT*4*ET*0 solid red line in Fig. 1b), sp^2 hybridized carbon at 284.58 eV dominates, with the sp^3 at 284.97 eV resulting from a combination of defects and adventitious carbon,[45] and a slight contribution from the C–O phenol group at 285.75 eV.[43] However, after only 1 min of etching (*ET*1) in an oxygen plasma (*AT*4*ET*1 open circles in Fig. 1c), the *C* 1*s* is dominated by the sp^3 hybridized carbon, with enhanced C–O signal. There is also an increase in the C=O group after etching in Fig. 1c with the peak height ratio of the C=O to the main peak for the non-etched (Fig. 1b) and 1-min-etched sample (Fig. 1c) doubling from 0.04 to 0.08. This ratio can be used to estimate the amount of oxygen incorporated in a graphene backbone, based on Nishina et al.'s study, in which a continuum of oxygen content in graphene oxide (GO) was differentiated using XPS.[44] One minute of etching resulted in an rGO-like structure with 27.8 wt% surface oxygen content, which maintains sufficient electrical conductivity to use in practical device applications.[44]

As ATR-FTIR is more sensitive to carbon functionalization, it was performed to identify the oxygen species obtained with various processing steps. In Fig. 1d, the peaks in the 3100–2800 cm^{-1} region belong to the CH$_2$ or CH$_3$ groups[48] whereas the peaks in the 800–1800 cm^{-1} region in Fig. 1e belong to the oxygen functional groups.[48] As pristine graphene should have no significant FTIR features,[49] the various functional groups identified with dotted lines show evidence of significant oxygen doping on graphene by plasma etching. Slight oxygen incorporation is also visible for the annealed sample, but significantly less than that for the pristine sample (*AT*0*ET*0), as would be expected for graphene on Cu with exposure to ambient air.[29] In keeping with our XPS findings that the oxygen content in the sample increased with short etching, the ATR-FTIR results show significantly increased oxygen functionalization for the *ET*1 sample after annealing compared to the *ET*0 sample, where there was clear hydroxyl and epoxy formation. As the pristine samples also show similar features, this supports our conclusion above that the sp^3 hybridized *C* 1s mostly originates from defects on the graphene surface. Further adjustment of this oxygen doping is possible with controlled plasma oxidation,[20,25] shown by the modification of the sample surface energy (Fig. 1f), decreasing the water contact angle from 82° to 51° after 1 min, to below 20° with longer plasma oxidation. Due to the scavenging nature of the Cu, longer etching times results in lower oxygen content in the resultant rGO-like layer, with ~20% oxygen doping with 90 min plasma exposure.[20]

This suggests that as long as the oxygen plasma etching is less than the CET, the resultant rGO-like layer will be an effective carrier layer for transferring nanoparticles, acting as a mechanical support with some conductivity. The CET for as-received graphene was previously determined to be roughly 17 min,[20,42] which is less than the 25 min plasma etching time required for RMD nanoparticles (dotted line in Fig. 2a). As shown in Fig. 2b, as-received graphene is not able to withstand the plasma etching required to remove the micelles. Typically, a ML of nanoparticles or loaded micelles are not visible under Raman and the spectrum is initially identical to a graphene layer, with a strongly visible G peak at 1580 cm^{-1}, corresponding to the first order degenerate phonon energy, E$_{2g}$, mode at the G point of graphene.[50] The 2D mode at 2690 cm^{-1} comes from the G mode overtone and is indicative of sp^2 hybridization,[51] suggesting high quality defect free graphene. After 25 min etching (*ET*25) in oxygen plasma, the resultant Raman spectrum (black dotted line) is featureless, indicating complete removal of the graphene layer.

However, as shown in Fig. 2a, and observed previously,[42] a dramatic increase in the CET is achieved with low temperature annealing from less than 20 min to over 2 h. Under these mild annealing conditions, after *ET*25, the Raman spectrum (dotted green line) show the expected "apparent" G mode (G$_{app}$) located at 1590 cm^{-1}. This G$_{app}$ is a broadened mode which contains both G and D′ (near 1620 cm^{-1}) modes.[52–55] The D′ is a defect activated intravalley one-phonon mode associated with the C–H sp^3 hybridization defect and the overtone of the D mode.[55–57] It also shows a feature from D at 1350 cm^{-1}, which is the defect-activated intervalley two-phonon mode for sp^3 defects,[50,53,55] as well as the 2D.[53]

Though the intensity ratio of D to G is often used to quantify the degree of defectiveness for graphene,[40,41,58,59] it is not a meaningful quantitative guide for the degree of defectiveness for graphene oxides.[20,43,52,54] As rGO and GO surfaces are quite inhomogeneous, most forms of rGO and GO show essentially the same D to G ratio, irrespective of oxygen doping levels,[20,43,52,54] Instead, to determine the nature of the resultant layer, we used the peak position difference of D′ to G$_{app}$, following the metric established by King et al.[52] With the G mode fixed at 1590 cm^{-1}, it was determined to be around 13 cm^{-1}, putting it in the regime for rGO-like structures, in keeping with our previous study[20] (see Hui et al.[20] for detailed description of the calculations and peak fitting parameters; example peak fitting is given in the supporting information Fig. A-3).

Therefore, using graphene as a mechanical support is not possible without a mild annealing step. We believe that this is due to surface contamination. Ambient air and other volatile organic compounds are known to contaminate graphene and graphite with radical modification of surface properties.[29–32,60] Li et al.[29] showed that as little as 20 min exposure to ambient air was enough to saturate the surface of a freshly grown CVD graphene on Cu with airborne hydrocarbons. We similarly observed an increase in the contact angle with 20 min aging in air of the etched sample, as shown in Fig. 1f.

To explain this mechanism, it is helpful to consider the process by which carbon based systems oxidize. Oxidation typically proceeds by the dissociation of C–H bonds to produce radical polymer species. An oxygen molecule can react at this site to form a peroxide radical which can then form a hyperoxide through reaction of adjacent carbons.[61] If there is sufficient energy, and a steady supply of oxygen, as in an oxygen plasma, these volatile fragments can instead cleave off, removing the hydrocarbon, through a chemical etching process.[62] As shown in Fig. 2a, and observed previously,[42] as little as 4 min of annealing dramatically increases the critical etching time from 17 to 190 mins; however, subsequent annealing does not significantly affect the CET. This plateau of enhancement suggests a mechanism that occurs at the very early stage of annealing, such as decontamination.

In plasma surface modifications, RF power is used to create chemically active species from a relatively inert molecular gas such as oxygen or argon. These reactive ions interact with surface species to form the volatile compounds.[63] Typically, the combination of ion bombardment to dissociate the bond with an inert gas, coupled with reactive chemical etching with volatile oxygen species, results in faster etching than either alone.[64] Therefore, either increased bond

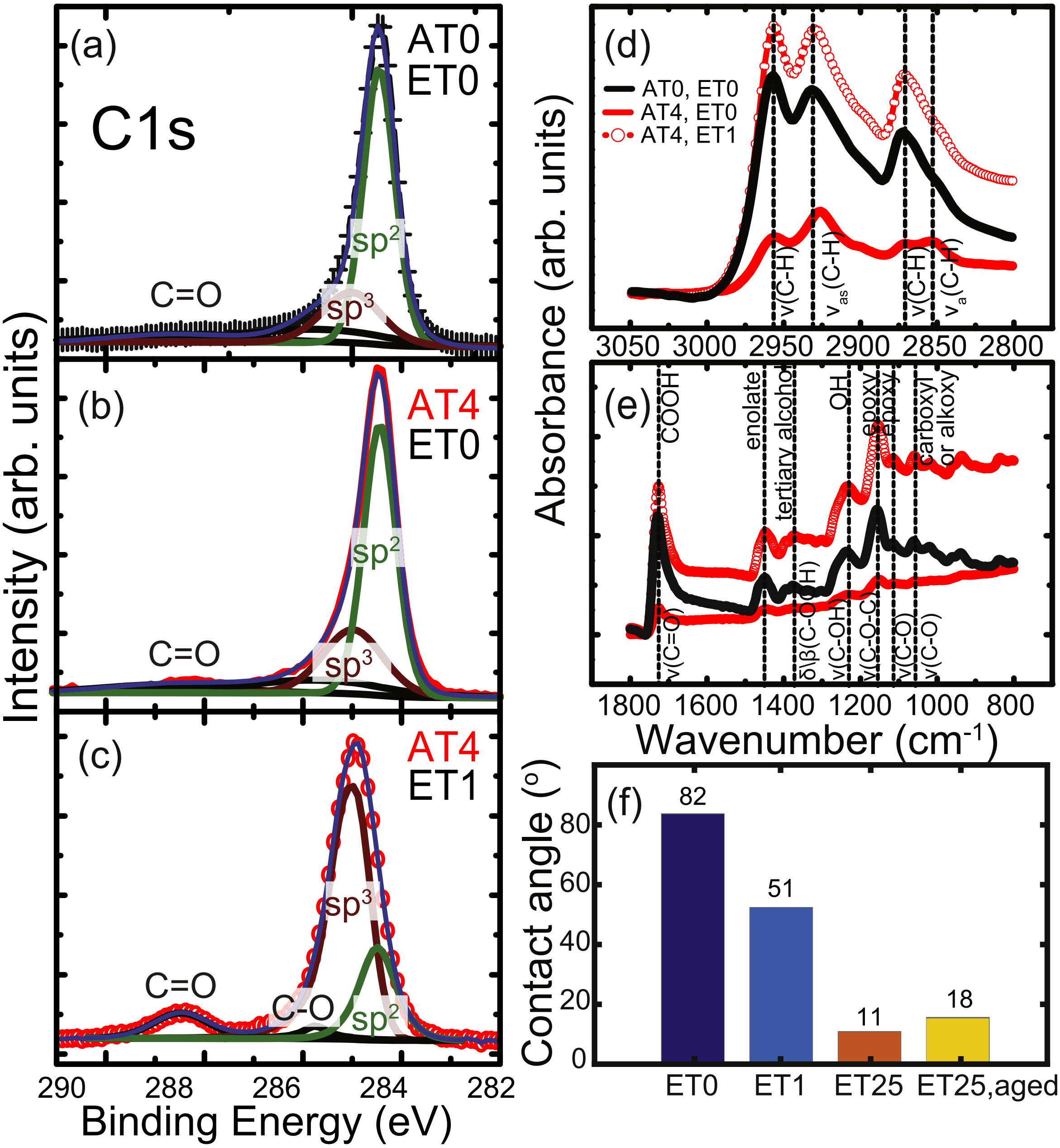

Figure 1. High resolution *C* 1*s* XPS spectra comparison of CVD full graphene on Cu (a) as-received (AT0, ET0), (b) annealed for 4 min at 180 °C (AT4) and (c) annealed AT4 then etched for 1 min (ET1). (d) and (e) Background subtracted ATR-FTIR spectra CVD full graphene annealed for AT4 mins at 180 °C and etched for 1 min, highlighting in (d) the stretching modes of CH_2 or CH_3 groups between 2800 and 3100 cm^{-1} and in (e) the stretch modes of oxygen functional groups between 800 and 1800 cm^{-1} at indicated by the dotted lines. Note that red lines correspond to samples that have been annealed (f) Contact angle measurements for samples annealed for 4 min at 180 °C (AT4), under various conditions of etching and aging.

dissociation or more abundant oxygen species will accelerate oxidation and trigger etching. If oxygen or surface species are already present at the surface, weakening the C–H bond though chemi- or physi-sorption, the initial bombardment to create dangling surface bonds does not need to occur, and the etching rate can be dramatically increased.

This contamination-assisted plasma etching action of CVD graphene on Cu is shown schematically in Fig. 2. The as-received sample initially has many hydrocarbon contaminants attached to the graphene surface (see Fig. 1). With the presence of these contaminants, exposure to the plasma rapidly over-etches the whole graphene sheet and it is completely cleaned off from the Cu substrate. However, when low temperature annealing is performed, hydrocarbon contaminant species are desorbed by the annealing, leaving a cleaner surface. In such a case, exposure to the plasma for the same length of time oxidizes the film rather than removing it by etching, producing an rGO-like film of controlled oxygen doping.

Ultraviolet-ozone (UV-O_3) treatment and high temperature (550 °C) thermal annealing in inert gases have been used previously to eliminate residues on graphene.[29] However, these methods have been known to alter the intrinsic properties of the graphene surface, such as introducing interlayer strain between graphene and Cu by high temperature annealing[65] and uncontrolled oxygen doping during the UV-O_3 treatment.[29,66] The mild annealing, on the other hand, desorbs the absorbed oxygen, without significantly affecting other graphene properties, as shown in Fig. 3.

ATR-FTIR was performed on graphene annealed for various times, showing the degree of decontamination systematically increases with annealing time. Figures 3a and 3b shows the ATR-FTIR absorbance spectra of the graphene during annealing up to 30 min,

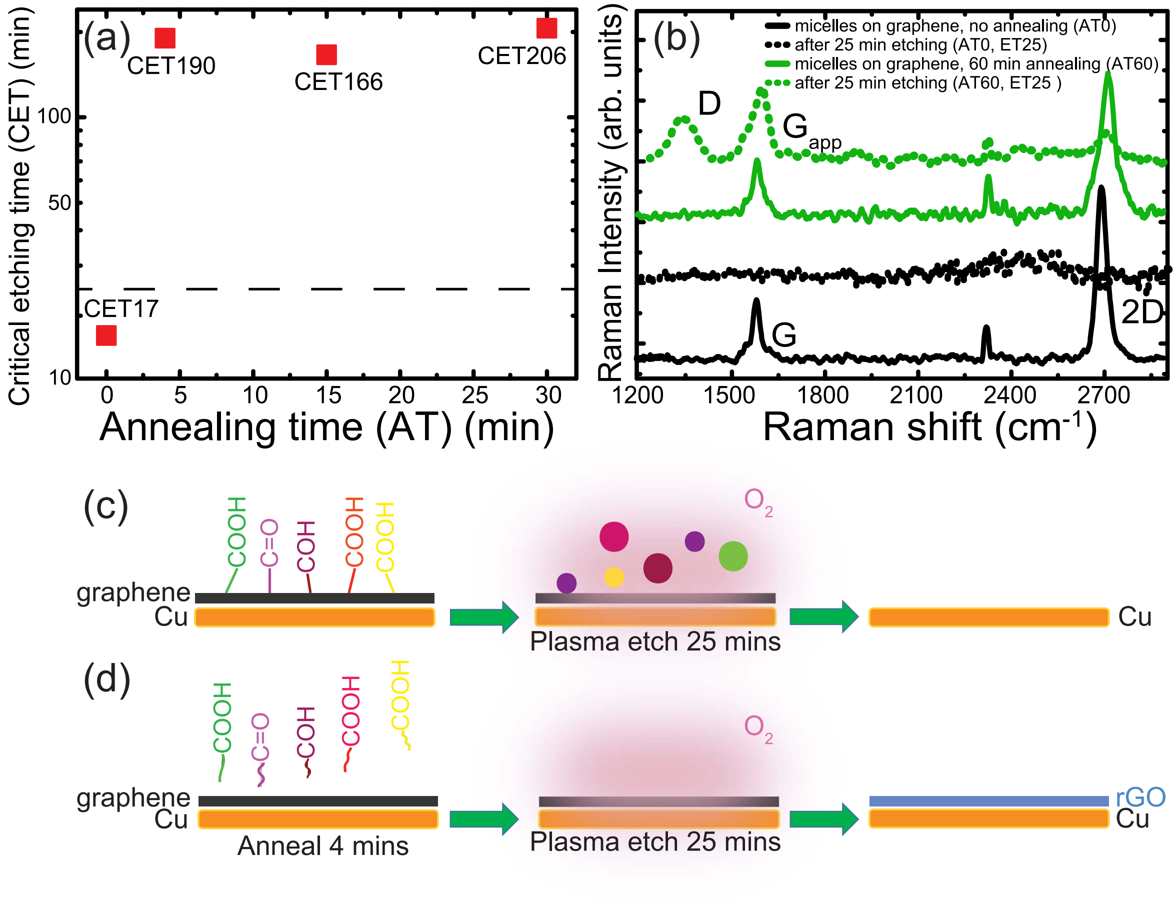

Figure 2. (a) Critical etching time (CET) required to completely remove all Raman features related to graphene for annealing times up to 30 min. Dotted line represents the 25 min etching (ET25) time required to remove the micelles and leave behind nanoparticles. (b) Raman spectra comparison of CVD full graphene on Cu (FG) with micelles, annealed for AT0 and AT60 mins at 180 °C (solid lines). Dotted lines show the samples after etching for ET25 to achieve nanoparticles. With ET25, which is above the CET for AT0, no Raman features from the graphene are visible (black dotted line); for AT60, where it is below the CET, the D and G_{app} peaks are visible, suggesting defected graphene is still present. The G_{app} is a convolution of the G and D′ peaks of functionalized graphene. (c) and (d) Schematic of oxygen plasma etching process of hydrocarbon contaminated CVD graphene on Cu for (c) untreated surface and (d) low-temperature annealed surface.

with oxygen functional groups identified with dotted lines. All the samples have the same aging conditions, having been synthesized at the same time and stored in a low humidity vacuum dessicator for the same period of time. In all cases, there is evidence of some degree of oxygen doping, as pristine graphene should have no significant FTIR features.[49] The as-recieved graphene *AT*0 (black solid line) shows the most significant signs of hydrocarbon contamination. The low temperature annealing treatment desorbed the contaminants as depicted in the schematic in Fig. 2d and hence the absorbance intensity of these oxygen functional groups dropped most significantly from *AT*0 (black solid line) to *AT*4 (red solid line) and continue to drop relatively less as annealing time progresses to *AT*15 (blue solid line) and *AT*30 (green solid line).

In particular, a peak around 1450 cm^{-1}, which we have previously assigned to the metal enolate group,[20,45,67] diminishes with increased annealing time. This group was identified as the driving force for synergistic oxidation,[20] where the strong intermixing of the *Cu* 3*d* electron states with the the *C* 2*p* electron states[68] opens up reactive pathways for Cu to scavenge the oxygen, leaving behind the carbon network. This simple process of low temperature annealing, therefore, is effective in desorbing oxygen and eliminating contaminants, such that when "clean" graphene is put under plasma etching, they oxidize and can persist much longer than untreated graphene, as seen by the dramatic increase in CET.

The water contact angle measurements also support this interpretation, showing initially water contact angles reflective of graphene exposed to ambient for extended periods[60] (see Fig. 3c). Even with temperatures as low as 180 °C, we see the large initial drop of contact angle after 4 min annealing, followed by a slight but steady decrease with annealing time.

Most importantly, this low temperature annealing treatment does not have major effect on the quality of the graphene layer. Figure 3d shows the Raman spectra for the unetched graphene samples with various annealing times, showing high quality defect free monolayer graphene, without any defect modes. Only tThe G peak at 1580 cm^{-1} of the E_{2g} mode at the G point[50] and the 2D overtone mode at 2690 cm^{-1} indicative of sp^2 hybridization[51] are visible. The 2D modes of all the annealed samples can be well fitted with a single Lorentzian peak shape with a similar full width at half maximum (FWHM), indicating that they are indeed defect free, and monolayer in most cases.[69] Traditionally, the peak area ratio of the 2D and G modes indicates the number of graphene layers.[50,69,70] The 2D/G ratio, varying between 3–4 except for AT15, shows no systematic effect from annealing. Measurements at various locations on the surface of each sample indicate a non-uniform surface with 2G/D ratios varying by roughly 10%; therefore, all values can be considered consistent with monolayer graphene. This is also supported by the XPS spectra, which show little change in the sp^2 hybridized fraction of carbon on the surface with annealing (Fig. 1), as also reported by others.[26] This suggests that the graphene is not modified by annealing at 180 °C.

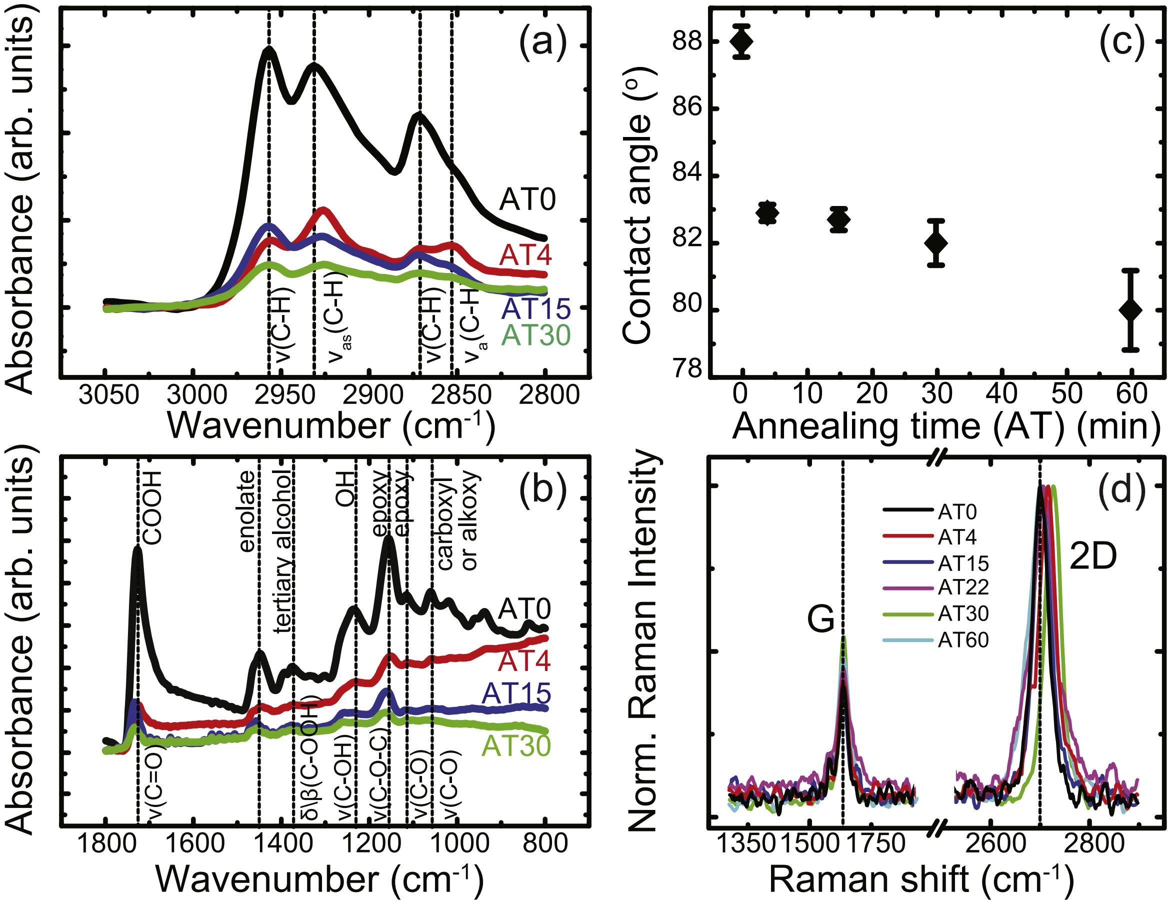

Figure 3. Background subtracted ATR-FTIR spectra CVD full graphene annealed for ATX mins at 180 °C, highlighting (a) the stretching modes of CH_2 or CH_3 groups between 2800 and 3100 cm^{-1} (b) the stretch modes of oxygen functional groups between 800 and 1800 cm^{-1} at indicated by the dotted lines (c) Contact angle measurements from sessile drop water droplets. (d) Raman spectra comparison of CVD full graphene on Cu annealed for ATX mins at 180 °C, normalized using the peak height of the 2D mode.

Though all spectra have a consistent peak position difference between G and 2D, there is a slight blueshift of the 2D band observed for all annealing times. Though this could be a characteristic of multi-layered graphene,[71] the expected accompanying peak broadening was not observed. Another possible explanation for the observed shift is a change of strain at the interface.[65,72,73] There is no systematic trend with annealing time, with the maximum strain relief around 0.38% (+25 cm^{-1}), calculated using the values reported for $\delta\omega_{2D}/\delta\epsilon$ of ~66 cm^{-1}/% strain for deposition induced tensile strain[65] and ~64 cm^{-1}/% for applied tensile strain.[72] As even 4 min of annealing show some strain relief, it is possible that surface reconstruction from strain relief plays a role in the oxidation of the graphene, as strain is known to enhance diffusion (see for example Spjut et al.[74]). Even unstrained, Cu is known to be highly mobile at room temperature, especially in the presence of carbon based molecules[75] or with oxygen.[76] A strained Cu surface from high temperature CVD growth would have even more mobile surface atoms at room temperature; with enhanced diffusion, the Cu may be able to scavenge the oxygen from the carbon surface more quickly and rapidly oxidize at defects. Annealing, therefore, could relax some of this strain, slowing down the synergistic oxidation of Cu and graphene[20] under extended plasma exposure. As the CET is maximized at AT30 (30 min annealing), this strain effect could also be an additional small factor of the resistance of the annealed graphene to complete etching.

With decontamination of the surface without affecting the monolayer film, it is now possible to control the oxygen doping during plasma oxidation. The Raman spectra for samples annealed for various times and etched in oxygen plasma for 25 min (*ET*25) are shown in Fig. 4a, normalized at the "apparent" G mode (G_{app}) located at 1590 cm^{-1}. All Raman spectra of the etched samples also show peaks from D at 1350 cm^{-1}. As expected, the ratio between G_{app} and D is approximately the same for all spectra, in keeping with the fact that most forms of rGO and GO show essentially the same D to G ratio, irrespective of oxygen doping levels.[20,43,52,54]

Using the peak position difference of D′ to G_{app} in Fig. 4b, we determined which type of graphene was formed for the same etching times. We made various attempts at deconvoluting the G_{app} mode by fixing different parameters; however, as the modes are all subject to natural shifting due to strain or sample variations, without a reference standard it is difficult to justify fixing a particular mode. If 2D′ modes (overtone of D′[53]) are present in the Raman spectrum, it may be possible to infer the D′ mode position, as was done by King et al.[52]; this mode, however, was not observed for any samples in this study. This is not uncommon for GO.[54] Kaniyoor et al.[54] failed to see any 2D′ modes but were still able to assign a D′ within the broad G envelop, aided by a tunable excitation wavelength. For convenience, we fixed the G mode at 1590 cm^{-1} for all samples in this study, as shown in supporting information Fig. A-3. As shown in Fig. 4b, the peak position difference of annealed samples varies from 12.8 to 17 cm^{-1}, all sitting within the rGO-like regime.[52] Under plasma treatment suitable to expose the nanoparticles from within the micelles, therefore, all of the annealed samples are functionalized to become rGO-like, in keeping with our previous study.[20]

As seen in Fig. 4a, the 2D mode intensity becomes stronger as annealing time increases, while the D mode remains almost the same, suggesting a greater degree of intact sp^2 hybridization with longer annealing times. It is worth noting that the 2D modes

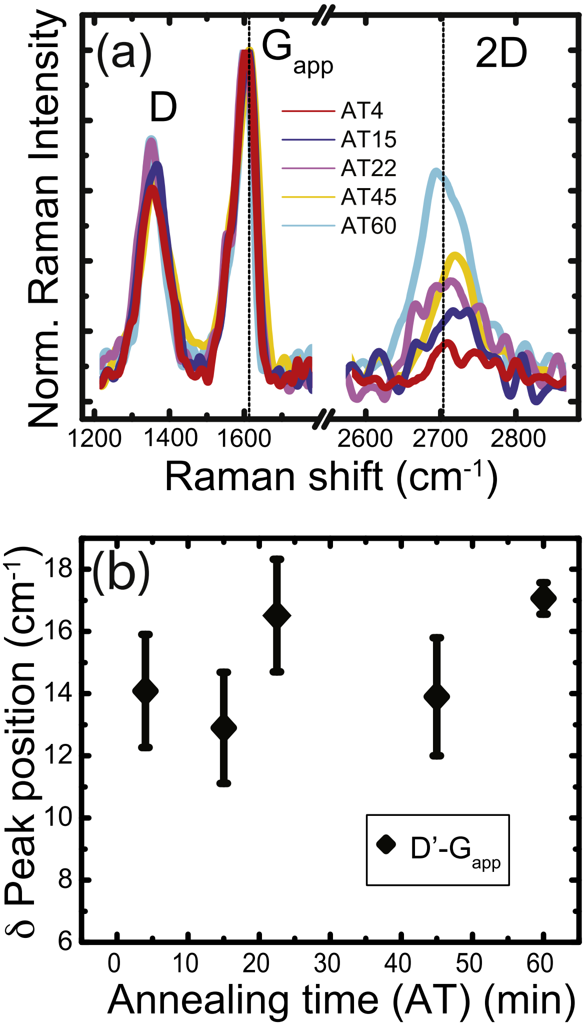

Figure 4. (a) Raman spectra comparison of CVD full graphene on Cu annealed for ATX mins at 180 °C and etched for 30 min showing the D, G_{app} and 2D peaks. Spectra normalized at the peak height of G_{app} mode, which is a convolution of the G and D′ peaks of functionalized graphene. (b) Peak position difference of D′ to G_{app} determined by deconvolution following the procedure described in Ref. 20.

experience some degree of red shifting as the *AT*X increases and the peak shape becomes more well-defined. The combination of exposure to plasma and annealing gives two vectors for controlling the oxygen doping profile in the activated graphene films on Cu.

As described in Fig. 2b, this behavior also holds when the micelles are spin-coated on the annealed graphene surfaces, though the level of intact sp^2 hybridized C (shown by the 2D peak) is slightly diminished. To confirm that the rGO-like layer is intact and strong enough to transfer nanoparticles onto the target organic layer after plasma etching, we performed a transfer printing with micelle templated LiF nanoparticles on the graphene layer. To maximize the decontamination and preserve the largest sp^2 hybridization, we chose an annealing time of 60 min (*AT*60), where there was still a visible 2D peak after etching, suggesting a high quality layer for transferring. This transfer-printed rGO-like layer with nanoparticles after plasma etching for *ET*25 mins can be seen in Fig. 5 on poly(3-hexylthiophene):[6,6]-phenyl C61-butyric acid methylester 1:1 blend (P3HT:PCBM).

Figure 5 shows the SNOM/AFM analysis of the edge of a transfer-printed rGO-like stack, with bare P3HT:PCBM on the left side of the topographical (AFM, panel a) and nano-optical (SNOM, panel b) images. The edge of the rGO layer is clearly visible from the AFM topography image, distinct from the P3HT:PCBM. From Fig. 5a, it can also be seen that the transfer printed stack increased the sample thickness by about 40–50 nm. Because <1-nm thick single-layer CVD graphene is used in our study, this suggests that the transfer-printed stack also includes a layer of LiF nanoparticles underneath, either surrounded by air or immersed in P3HT:PCBM. This hypothesis is substantiated by the quantitative analysis of the near-field radiation attenuation from the SNOM image. Figure 5b shows that the SNOM signal extinction is much stronger (80 kcts s^{-1} more, on average) in the area where graphene was transferred. As the PMT count rate at 100% transmission is $I_0 = 350 \pm 50$ kcts s^{-1} in the used measurement conditions, this corresponds to a transmittance $22 \pm 5\%$ lower than P3HT:PCBM, as shown in Fig. 5c. Because single-layer graphene possesses ∼98% transmittance and minimal surface reflectivity[77] this effect is unlikely to come from the rGO-like sheet.

LiF nanoparticles, which are situated beneath the rGO-like sheet, are strong light scatterers due to their high surface-to-volume ratios, and may be responsible for the strong diffuse reflectance associated with the observed decrease in transmittance. Because the in-depth sensitivity of SNOM measurements is about 90 nm, this nano-optical tool is highly sensitive to the presence of subsurface LiF nanoparticles. Therefore, although the ability of functionalized graphene to transfer-print LiF cannot be directly validated by AFM, it can be successfully mapped via SNOM. To quantify these observations we notice that, for near-field scattered, far-field collected radiation, the extinction cross section is given by Ref. 78:

$$Q_{ext} = 4\frac{\pi n_o D}{\lambda}\,\mathrm{Im}\left\{\frac{(n/n_o)^2 - 1}{(n/n_o)^2 + 2}\right\} + \frac{8}{3}\left(\frac{\pi n_o D}{\lambda}\right)^4 \times \mathrm{Re}\left\{\frac{(n/n_o)^2 - 1}{(n/n_o)^2 + 2}\right\} \qquad [1]$$

where n_o and n are the refractive indexes, respectively, of the background medium and the nanoparticles that are modelled to be spherical with diameter $D \ll \lambda$. The λ^{-1} addend in Eq. 1 represents the contribution from light absorption, which is only present if either n or n_o are complex, while the λ^{-4} addend, reminiscent of Rayleigh scattering, represents the contribution from diffuse reflectance.[78] As no more than one particle monolayer is expected, multiple reflections are neglected as a first-order approximation.

Figure 5d simulates the attenuation of the collected SNOM signal as a function of the LiF nanoparticle diameter assuming $n(\lambda) = 1.39$ for LiF,[79] and $n_o(\lambda) = 1$ or $2.04 + i0.69$[80] for nanoparticles embedded in air or P3HT:PCBM, respectively. A remarkable agreement between SNOM signal attenuation and thickness-volume increase inferred by AFM is observed for $D \approx 30$ nm, which also coincides with the LiF particle diameter observed prior to transfer printing (see supporting information Fig. A-1). As this agreement is obtained using the refractive index of P3HT:PCBM as the background medium, we conclude that the LiF nanoparticles have interpenetrated the soft P3HT:PCBM layer during the printing process, thus displacing a significant amount of organic material. Furthermore, the histogram in Fig. 5c shows that the SNOM signal attenuation is not uniform all through the image, with a bimodal distribution for the LiF/rGO-like coated region. This can be assigned to a non-uniform distribution of LiF nanoparticles, with more transparent regions in which they are sparser, or totally absent, with the minimum peak-to-peak difference between coated and uncoated regions corresponding to a 2% transmittance decrease consistent with a bare graphene layer. We can therefore conclude that a combination of oxygen plasma exposure and annealing represents a unique tool for transfer-printing not only bare graphene, but also nanoparticle-functionalized rGO-like layers, and the nanoparticle distribution under graphene can be usefully monitored and mapped via a combined SNOM/AFM approach.

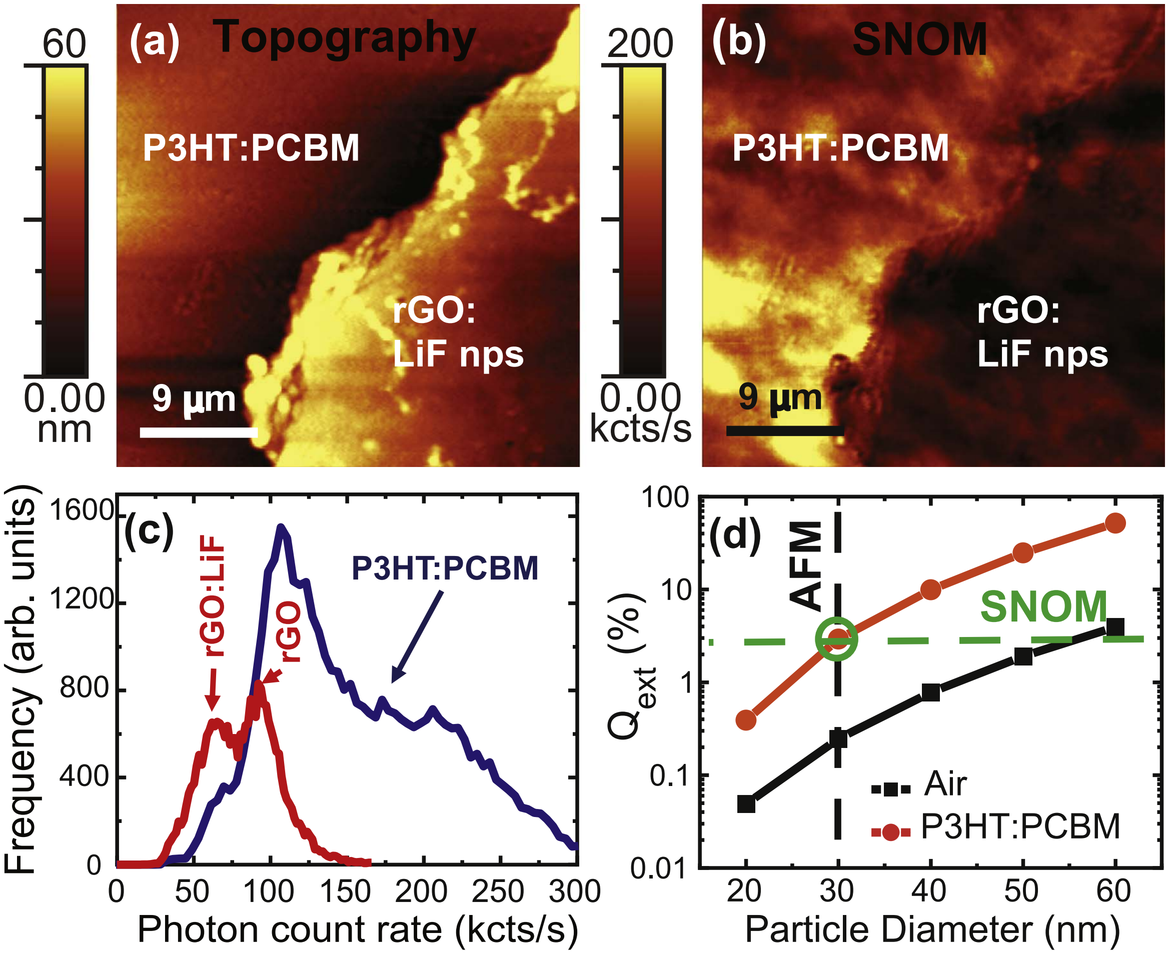

Figure 5. (a) Contact mode atomic force microscopy (AFM) and (b) aperture-type transmission mode scanning near-field optical microscopy (SNOM) images at 532 nm obtained at the edge between bare P3HT:PCBM and transfer-printed rGO-like layer. AFM shows that the coated region is significantly thicker than the single-layer rGO-like material used for transfer printing, while SNOM indicates it is significantly less transmissive, with both effects suggesting that a layer of LiF nanoparticles has been transferred along with graphene. (c) SNOM signal histogram obtained from panel (b) showing a broad distribution for the bare P3HT:PCBM region and a narrower but bimodal distribution for the rGO-like coated region, corresponding, respectively, to a 2% transmittance decrease over the P3HT:PCBM peak (consistent with bare graphene) and a significantly less transmissive region (60 kcts s^{-1} peak). (d) simulations based on Eq. 1 show that this region is consistent with near-field light scattering from 30-nm diameter LiF nanoparticles embedded in a P3HT:PCBM background medium, in agreement with the thickness increase observed in panel (a) by AFM.

Conclusions

Low temperature annealing in air of CVD graphene on Cu is found to be effective in removing hydrocarbon contaminants accumulated on the surface, without changing the initial graphene characteristics as has been a problem in other decontamination approaches. This increases the resistance of the graphene film to oxygen plasma etching, making it suitable as a mechanical support to transfer reverse micelle templated nanoparticles onto organic surfaces. A brief annealing treatment can provide enough energy to desorb the contaminants on the surface, as seen by ATR-FTIR and water contact angle measurements, without changing the sp^2 hybridization of graphene as shown by XPS and Raman measurements. When hydrocarbon contaminant species are desorbed by annealing, exposure of the CVD graphene to the plasma oxidizes the film rather than etching it, producing an activated graphene film of controlled oxygen doping, making it suitable for incorporation into devices. Introducing micelles on the graphene surface modifies the etching process slightly, but still results in an intact rGO-like layer. Upon transfer printing to an organic surface, the nanoparticles are embedded in the organic surface, sandwiched beneath the rGO-like layer, making them ideal as an interlayer in organic devices. The addition of an annealing step results in a universal activated graphene carrier layer with nanoparticles, where the combination of exposure to plasma and annealing gives two vectors for controlling the oxygen doping profile, and suggests new avenues for patterning nanostructures in devices with processing sensitive active layers.

Acknowledgments

The authors thank Dr. Danielle Covelli at the Biointerfaces Institute at McMaster for ATR-FTIR measurements, MMRI for access to the AFM for measurements, Dr. Rana Sodhi at Surface Interface Ontario and Dr. Alex Adronov for Raman instrument time. We would also like to thank Jacob Bresoli for the help with the contact angle measurements. We acknowledges financial support from the Ontario Ministry of Research and Innovation (ER15-11-123) for A.T., the Canada Research Chair secretariat for G.F and the Natural Sciences and Engineering Council of Canada (RGPIN-2019-05994, 436 100-2013 RGPIN, 384 889-2010 CREAT for A.T., RGPIN-2014-05004 and RGPIN-2020-56679 for G.F). VW acknowledges an NSERC-PGS Scholarship.

ORCID

A. Turak https://orcid.org/0000-0002-2038-0624

References

1. H. Mizuno, T. Kaneko, I. Sakata, and K. Matsubara, *Chem. Commun.*, **50**, 362 (2014).
2. T. H. Kim et al., *Nat. Photonics*, **5**, 176 (2011).
3. A. Turak, T. Aytun, and C. W. Ow-Yang, *Appl. Phys. Lett.*, **100**, 253303 (2012).
4. T. Aytun, A. Turak, I. Baikie, G. Halek, and C. W. Ow-Yang, *Nano Lett.*, **12**, 39 (2012).
5. S. I. Lee, G. J. Yun, J. W. Kim, G. Hanta, K. Liang, L. Kojvic, L. S. Hui, A. Turak, and W. Y. Kim, *Sci. Rep.*, **9**, 2411 (2019).
6. X. Gu, T. Qiu, W. Zhang, and P. K. Chu, *Nanoscale Res. Lett.*, **6**, 199 (2011).
7. H. A. Atwater and A. Polman, *Nat. Mater.*, **9**, 205 (2010).
8. E. Ozbay, *Science*, **311**, 189 (2006).
9. K. Liang, L. Shu Hui, and A. Turak, *Nanoscale*, **11**, 9076 (2019).
10. L. S. Hui et al., *ACS Appl. Nano Mater.*, **2**, 4121 (2019).
11. S. M. Stavis, J. A. Fagan, M. Stopa, and J. A. Liddle, *ACS Appl. Nano Mater.*, **1**, 4358 (2018).
12. J. W. Jeong, W. I. Park, L. M. Do, J. H. Park, T. H. Kim, G. Chae, and Y. S. Jung, *Adv. Mater.*, **24**, 3526 (2012).
13. S. K. Abkenar, A. Tufani, G. O. Ince, H. Kurt, A. Turak, and C. W. Ow-Yang, *Nanoscale*, **9**, 2969 (2017).
14. C. Wang, K. Ryu, A. Badmaev, N. Patil, A. Lin, S. Mitra, H. S. P. Wong, and C. Zhou, *Appl. Phys. Lett.*, **93**, 033101 (2008).
15. K. Ryu, A. Badmaev, C. Wang, A. Lin, N. Patil, L. Gomez, A. Kumar, S. Mitra, H. S. P. Wong, and C. Zhou, *Nano Lett.*, **9**, 189 (2009).
16. T. W. Odom, J. C. Love, D. B. Wolfe, K. E. Paul, and G. M. Whitesides, *Langmuir*, **18**, 5314 (2002).
17. K. S. Kim, Y. Zhao, H. Jang, S. Y. Lee, J. M. Kim, K. S. Kim, J. H. Ahn, P. Kim, J. Y. Choi, and B. H. Hong, *Nature*, **457**, 706 (2009).
18. X. Li, Y. Zhu, W. Cai, M. Borysiak, B. Han, D. Chen, R. D. Piner, L. Colombo, and R. S. Ruoff, *Nano Lett.*, **9**, 4359 (2009).
19. X. Liang et al., *ACS Nano*, **5**, 9144 (2011).
20. L. S. Hui, E. Whiteway, M. Hilke, and A. Turak, *Carbon*, **125**, 500 (2017).
21. C. M. Seah, B. Vigolo, S. P. Chai, and A. R. Mohamed, *Carbon*, **105**, 496 (2016).
22. E. Starodub, N. C. Bartelt, and K. F. McCarty, *J. Phys. Chem. C*, **114**, 5134 (2010).
23. N. A. Vinogradov, K. Schulte, M. L. Ng, A. Mikkelsen, E. Lundgren, N. Mårtensson, and A. B. Preobrajenski, *J. Phys. Chem. C*, **115**, 9568 (2011).
24. R. Larciprete, S. Fabris, T. Sun, P. Lacovig, A. Baraldi, and S. Lizzit, *J. Am. Chem. Soc.*, **133**, 17315 (2011).
25. T. Gokus, R. R. Nair, A. Bonetti, M. Böhmler, A. Lombardo, K. S. Novoselov, A. K. Geim, A. C. Ferrari, and A. Hartschuh, *ACS Nano*, **3**, 3963 (2009).
26. C. Mattevi, G. Eda, S. Agnoli, S. Miller, K. A. Mkhoyan, O. Celik, D. Mastrogiovanni, G. Granozzi, E. Garfunkel, and M. Chhowalla, *Adv. Funct. Mater.*, **19**, 2577 (2009).
27. P. V. Kumar, M. Bernardi, and J. C. Grossman, *ACS Nano*, **7**, 1638 (2013).
28. C. T. Chien et al., *Angew. Chem. Int. Ed.*, **51**, 6662 (2012).
29. Z. Li et al., *Nat Mater*, **12**, 925 (2013).
30. D. Martinez-Martin, R. Longuinhos, J. G. Izquierdo, A. Marele, S. S. Alexandre, M. Jaafar, J. M. Gómez-Rodríguez, L. Bañares, J. M. Soler, and J. Gomez-Herrero, *Carbon*, **61**, 33 (2013).
31. V. Panchal, C. E. Giusca, A. Lartsev, N. A. Martin, N. Cassidy, R. L. Myers-Ward, D. K. Gaskill, and O. Kazakova, *2D Mater.*, **3**, 015006 (2016).
32. Y. Yang, K. Brenner, and R. Murali, *Carbon*, **50**, 1727 (2012).
33. P. J. Smith and P. M. Lindley, *AIP Conf. Proc.*, **449**, 133-139 (1998).
34. A. Afshari, L. Gunnarsen, P. A. Clausen, and V. Hansen, *Indoor Air*, **14**, 120 (2004).
35. P. Sun, C. Ayre, and M. Wallace, *AIP Conf. Proc.*, **683**, 245-253 (2003).
36. N. Lisi, T. Dikonimos, F. Buonocore, M. Pittori, R. Mazzaro, R. Rizzoli, S. Marras, and A. Capasso, *Sci. Rep.*, **7**, 9927 (2017).
37. X. Feng et al., *Carbon*, **87**, 78 (2015).
38. P. Bazylewski, S. Ezugwu, and G. Fanchini, *Appl. Sci.*, **7**, 973 (2017).
39. S. J. Moss, A. M. Jolly, and B. J. Tighe, *Plasma Chem Plasma Process*, **6**, 401 (1986).
40. I. Childres, L. A. Jauregui, J. Tian, and Y. P. Chen, *New J. Phys.*, **13**, 025008 (2011).
41. A. Eckmann, A. Felten, A. Mishchenko, L. Britnell, R. Krupke, K. S. Novoselov, and C. Casiraghi, *Nano Lett.*, **12**, 3925 (2012).
42. L. S. Hui, E. Whiteway, M. Hilke, and A. Turak, *Faraday Discuss.*, **173**, 79 (2014).
43. D. Yang et al., *Carbon*, **47**, 145 (2009).
44. N. Morimoto, T. Kubo, and Y. Nishina, *Sci. Rep.*, **6**, 21715 (2016).
45. P. R. Kidambi, B. C. Bayer, R. Blume, Z. J. Wang, C. Baehtz, R. S. Weatherup, M. G. Willinger, R. Schloegl, and S. Hofmann, *Nano Lett.*, **13**, 4769 (2013).
46. A. Siokou, F. Ravani, S. Karakalos, O. Frank, M. Kalbac, and C. Galiotis, *Appl. Surf. Sci.*, **257**, 9785 (2011).
47. C. Hontoria-Lucas, A. J. Lopez-Peinado, J. d. D. López-González, M. L. Rojas-Cervantes, and R. M. Martin-Aranda, *Carbon*, **33**, 1585 (1995).
48. I. Wlasny, P. Dabrowski, M. Rogala, P. J. Kowalczyk, I. Pasternak, W. Strupinski, J. M. Baranowski, and Z. Klusek, *Appl. Phys. Lett.*, **102**, 111601 (2013).
49. V. Ţucureanu, A. Matei, and A. M. Avram, *Crit. Rev. Anal. Chem.*, **46**, 502 (2016).
50. A. C. Ferrari et al., *Phys. Rev. Lett.*, **97**, 187401 (2006).
51. G. H. Lee et al., *Science*, **340**, 1073 (2013).
52. A. A. K. King, B. R. Davies, N. Noorbehesht, P. Newman, T. L. Church, A. T. Harris, J. M. Razal, and A. I. Minett, *Sci. Rep.*, **6**, 19491 (2016).
53. A. C. Ferrari and D. M. Basko, *Nat. Nano*, **8**, 235 (2013).
54. A. Kaniyoor and S. Ramaprabhu, *AIP Adv.*, **2**, 032183 (2012).
55. M. Bruna, A. K. Ott, M. Ijäs, D. Yoon, U. Sassi, and A. C. Ferrari, *ACS Nano*, **8**, 7432 (2014).
56. L. Gao, J. R. Guest, and N. P. Guisinger, *Nano Lett.*, **10**, 3512 (2010).
57. J. Cho et al., *ACS Nano*, **5**, 3607 (2011).
58. A. Zandiatashbar, G. H. Lee, S. J. An, S. Lee, N. Mathew, M. Terrones, T. Hayashi, C. R. Picu, J. Hone, and N. Koratkar, *Nat. Commun.*, **5**, 3186 (2014).
59. L. G. Cançado, A. Jorio, E. H. M. Ferreira, F. Stavale, C. A. Achete, R. B. Capaz, M. V. O. Moutinho, A. Lombardo, T. S. Kulmala, and A. C. Ferrari, *Nano Lett.*, **11**, 3190 (2011).
60. A. I. Aria, P. R. Kidambi, R. S. Weatherup, L. Xiao, J. A. Williams, and S. Hofmann, *J. Phys. Chem. C*, **120**, 2215 (2016).
61. J. P. Luongo, *J. Polym. Sci.*, **42**, 139 (1960).
62. C. Corbella, S. Große-Kreul, and A. von Keudell, *Plasma Process. Polym.*, **12**, 564 (2015).
63. J. W. Coburn and H. F. Winters, *J. Vac. Sci. Technol.*, **16**, 391 (1979).
64. A. von Keudell and C. Corbella, *J. Vac. Sci. Technol. A*, **35**, 050801 (2017).
65. V. Yu, E. Whiteway, J. Maassen, and M. Hilke, *Phys. Rev. B*, **84**, 205407 (2011).
66. J. Seo, W. S. Chang, and T. S. Kim, *Thin Solid Films*, **584**, 170 (2015).
67. J. Comelles, M. Moreno-Mañas, E. Pérez, A. Roglans, R. M. Sebastián, and A. Vallribera, *J. Org. Chem.*, **69**, 6834 (2004).
68. J. Jung, H. Lim, J. Oh, and Y. Kim, *J. Am. Chem. Soc.*, **136**, 8528 (2014).
69. A. C. Ferrari, *Solid State Commun*, **143**, 47 (2007).
70. W. Liu, H. Li, C. Xu, Y. Khatami, and K. Banerjee, *Carbon*, **49**, 4122 (2011).
71. L. Malard, M. Pimenta, G. Dresselhaus, and M. S. Dresselhaus, *Phys. Rep.*, **473**, 51 (2009).
72. T. M. G. Mohiuddin et al., *Phys. Rev. B*, **79**, 205433 (2009).
73. Y. Y. Wang, Z. H. Ni, T. Yu, Z. X. Shen, H. M. Wang, Y. H. Wu, W. Chen, and A. T. Shen Wee, *J. Phys. Chem. C*, **112**, 10637 (2008).
74. H. Spjut and D. A. Faux, *Surf. Sci.*, **306**, 233 (1994).
75. F. Rosei, M. Schunack, P. Jiang, A. Gourdon, E. Lægsgaard, I. Stensgaard, C. Joachim, and F. Besenbacher, *Science*, **296**, 328 (2002).
76. R. Frerichs and I. Liberman, *Phys. Rev.*, **121**, 991 (1961).
77. R. R. Nair, P. Blake, A. N. Grigorenko, K. S. Novoselov, T. J. Booth, T. Stauber, N. M. R. Peres, and A. K. Geim, *Science*, **320**, 1308 (2008).
78. C. F. Bohren and D. R. Huffman, *Absorption and Scattering of Light by Small Particles* (Wiley-VCH, Weinheim) (1998).
79. C. Stelling, C. R. Singh, M. Karg, T. A. F. König, M. Thelakkat, and M. Retsch, *Sci. Rep.*, **7**, 42530 (2017).
80. H. H. Li, *J. Phys. Chem. Ref. Data*, **5**, 329 (1976).